Elliptic instability in a strained Batchelor vortex

LAURENT LACAZE[1], KRIS RYAN[2]
AND STÉPHANE LE DIZÈS[1]

[1]Institut de Recherche sur les Phénomènes Hors Équilibre (IRPHE), CNRS/Universités
Aix-Marseille I & II, 49 rue F. Joliot-Curie, BP 146, F-13384 Marseille cedex 13, France

[2]Fluids Laboratory for Aeronautical and Industrial Research (FLAIR), Department of Mechanical
Engineering, Monash University, Melbourne, Victoria 3800, Australia

The elliptic instability of a Batchelor vortex subject to a stationary strain field is considered by theoretical and numerical means in the regime of large Reynolds number and small axial flow. In the theory, the elliptic instability is described as a resonant coupling of two quasi-neutral normal modes (Kelvin modes) of the Batchelor vortex of azimuthal wavenumbers m and $m + 2$ with the underlying strain field. The growth rate associated with these resonances is computed for different values of the azimuthal wavenumbers as the axial flow parameter is varied. We demonstrate that the resonant Kelvin modes $m = 1$ and $m = -1$ which are the most unstable in the absence of axial flow become damped as the axial flow is increased. This is shown to be due to the appearance of a critical layer which damps one of the resonant Kelvin modes. However, the elliptic instability does not disappear. Other combinations of Kelvin modes $m = -2$ and $m = 0$, then $m = -3$ and $m = -1$ are shown to become progressively unstable for increasing axial flow. A complete instability diagram is obtained as a function of the axial flow parameter for several values of the strain rate and Reynolds number.

The numerical study considers a system of two counter-rotating Batchelor vortices in which the strain field felt by each vortex is due to the other vortex. The characteristics of the most unstable linear modes developing on the frozen base flow are computed by direct numerical simulations for two axial flow parameters and compared to the theory. In both cases, a very good agreement is obtained for the most unstable modes. Less unstable modes are also identified in the numerics and shown to correspond to peculiar resonances involving Kelvin modes from branches of different labels.

1. Introduction

A vortex which is elliptically deformed by an external strain field is generically subjected to the so-called elliptic instability. This instability has been extensively studied in vortices without axial flow. The purpose of this work is to analyse the effect of an axial flow on its occurrence and determine the elliptic stability characteristics of a classical model of a vortex with an axial jet.

The elliptic instability is now recognized as an important phenomenon of vortex dynamics. It is believed to take place in various contexts ranging from three-dimensional transition in shear flows (Bayly, Orszag & Herbert 1988) to vortex interactions (Leweke & Williamson 1998) and flows in elliptic containers (Eloy, Le Gal & Le Dizès 2003). We refer to the review by Kerswell (2002) for details and other references. The generic aspects of the elliptic instability were first identified by

Pierrehumbert (1986) and Bayly (1986) who considered the local stability properties of an elliptic flow. Before these local analyses, Moore & Saffman (1975) and Tsai & Widnall (1976) had identified an instability which develops in strained vortices. They performed the first global stability analysis of the elliptic instability and provided an instability mechanism in terms of normal mode resonance. Moore & Saffman (1975) showed, for an arbitrary strained vortex without axial flow, that two neutral normal modes (Kelvin waves) of the underlying axisymmetric vortex are coupled by the strain field if their characteristics satisfy a condition of resonance. They also provided, by an asymptotic analysis in the limit of small strain field, a formal expression for the complex growth rate of the resonant modes. This theory has been applied to various vortices without axial flow (Tsai & Widnall 1976; Eloy & Le Dizès 1999, 2001; Fabre & Jacquin 2004*a*).

The effect of axial flow has been considered in Lacaze, Birbaud & Le Dizès (2005) for the Rankine vortex with a constant axial flow in its core. They showed that axial flow modifies the characteristics of the most unstable resonant modes. However, the Rankine vortex is a crude approximation for a realistic vortex. In particular, we now know that some of its normal modes disappear when the vortex profile is changed into a smoothly varying profile (Sipp & Jacquin 2003; Fabre, Sipp & Jacquin 2006). The vortex we consider here is a classical model of a vortex with an axial flow. It is known to model correctly the structure of trailing vortices in the far-wake of aircraft (Batchelor 1964).

In the aeronautical context, the elliptic instability is expected to intervene in the dynamics of the multiple vortices generated by aircraft wings. Each vortex is in the strain field of surrounding vortices, and therefore subjected to an elliptic instability. In configurations without an axial flow, the elliptic instability has been observed experimentally in both counter-rotating vortices (Leweke & Williamson 1998) and in co-rotating vortices (Meunier & Leweke 2005). It has been modelled using Moore & Saffman's approach in Le Dizès & Laporte (2002). They demonstrated that this approach based on a single strained vortex provides very good estimates for the elliptic instability characteristics in vortex pairs. In the present work, a similar comparison will be performed: the theory constructed for a single strained vortex will be validated by numerical results obtained for a pair of counter-rotating Batchelor vortices.

The Batchelor vortex has been the subject of numerous works. It is known to be unstable with respect to inviscid perturbations when the axial flow exceeds a critical value (see for instance Ash & Khorrami 1995). Here, the axial flow will be varied below this critical value. The strong inviscid instability will not be active, allowing the development of the weaker elliptic instability. Fabre & Jacquin (2004*b*) have discovered that Batchelor vortices also exhibit unstable modes for small axial flow if the Reynolds number is sufficiently large. These modes are purely viscous and localized in the vortex centre. Their growth rate is $O(Re^{-1/3})$. They will not be considered in the present work. We shall consider the resonant coupling of inviscid normal modes only. For small axial flow velocities, these normal modes are expected to be either neutral or damped by a critical layer singularity. The appearance of critical layers is a common feature of normal modes in vortices with continuous vorticity profiles, but very little information is available in the literature. Sipp & Jacquin (2003) studied these singular modes for the Lamb–Oseen vortex. Le Dizès & Lacaze (2005) provided partial information on these modes for the Batchelor vortex using an asymptotic approach. An important part of the present work will be the determination of these modes for the Batchelor vortex as the axial flow velocity is varied.

The paper is organized as follows. In §2, the base flow and characteristic features of the Batchelor Kelvin modes are described. In §3, the theoretical results for the elliptic instability are presented. The inviscid characteristics of the first principal modes associated with resonance of Kelvin modes with the same branch labels are first given. The damping rate due to the critical layer is in particular calculated. The perturbation method leading to the elliptic complex growth rate formula is then briefly described in §3.2. The variation of each term in that formula for the different principal modes is analysed. Growth rate contour plots in the axial flow parameter – axial wavenumber plane are computed for several Reynolds numbers and strain rates. Instability diagrams showing the most unstable principal mode as functions of the Reynolds number and axial flow are also provided. The theory is compared to numerics in §4 where the instability characteristics of counter-rotating Batchelor vortices are computed. The numerical procedure and information on the code are first provided in §4.1 and §4.2, respectively. In §4.3, instability growth rates are computed versus the axial wavenumber for two different values of the axial flow. The characteristics of the theoretical principal modes are shown to be recovered with very good agreement. Other instability modes are also obtained and shown to be associated with non-principal modes (i.e. with resonant Kelvin modes of different branch labels). A brief conclusion is provided in the last section.

2. Problem formulation

2.1. *Description of the base flow field*

The Batchelor vortex is a self-similar solution of the Navier–Stokes equations. Its axial vorticity ω_0 and axial velocity W_0 can be written in cylindrical coordinates as

$$\omega_0 = \frac{\Gamma}{\pi R^2} \exp(-(r/R)^2), \qquad (2.1)$$

$$W_0 = \frac{\xi R_0^2}{R^2} \exp(-(r/R)^2), \qquad (2.2)$$

where the radius $R(t)$ evolves in time by viscous diffusion according to

$$R(t) = \sqrt{4\nu t + R_0^2}. \qquad (2.3)$$

The circulation Γ and axial velocity ξ are constants which measure the strengths of the rotation and of the jet, respectively.

In the following, the viscous diffusion of the radius $R(t)$ will be neglected and we will assume $R(t) = R_0$. This hypothesis is common in aeronautical applications where the Reynolds number often exceeds 10^6. In the numerical computation in §4, the base flow is artificially frozen.

Variables are non-dimensionalized by the radius R_0 and the angular velocity in the vortex centre $\Omega_0 = \Gamma/(2\pi R_0^2)$ such that the above expressions become:

$$\omega_0 = 2 \exp(-r^2), \qquad (2.4)$$
$$W_0 = W_0 \exp(-r^2). \qquad (2.5)$$

The flow is characterized by the Reynolds number $Re = \Gamma/(2\pi\nu)$ and the axial velocity strength $W_0 = 2\pi R_0 \xi/\Gamma$. The parameter W_0 is related to the Swirl number S, defined as the ratio of the maximum azimuthal velocity to the maximum axial velocity via the relation $W_0 = 0.638/S$ (Lessen, Singh & Paillet 1974).

Here, we shall assume that $W_0 < 0.6$ such that the vortex can be considered as stable in a inviscid framework (see Ash & Khorrami 1995). Unstable inviscid centre modes have recently been obtained for $W_0 < 0.6$, but their growth rate is so small that they should not intervene in the present study (Heaton 2007).

When a vortex is subjected to an external stationary strain field generated either by another vortex or by boundaries, its streamlines are deformed elliptically at leading order. The way an equilibrium solution is obtained when the strain field is small has been analysed in Jiménez, Moffatt & Vasco (1996) and Le Dizès (2000a) for a single strained vortex without axial flow, and in Sipp, Jacquin & Cossu (2000) for a system of two counter-rotating vortices without axial flow. The presence of an axial flow does not modify the two-dimensional equilibrium solution because the dynamics of the axial velocity is decoupled from the other components of the velocity. If we assume that the dimensionless external strain rate ε is small, a first-order solution for the axial vorticity and for the axial velocity can be obtained as

$$\omega_z = \omega_0 - \varepsilon \frac{f(r)\omega_0'}{2\Omega_0 r} \cos(2\theta) + O(\varepsilon^2), \qquad (2.6)$$

$$U_z = W_0 - \varepsilon \frac{f(r)W_0'}{2\Omega_0 r} \cos(2\theta) + O(\varepsilon^2). \qquad (2.7)$$

where $\Omega_0 = (1 - \exp(-r^2)/r^2$ is the angular velocity of the Batchelor vortex, ω_0 and W_0 have been defined in (2.4) and (2.5), respectively, and $f(r)$ satisfies

$$\frac{\mathrm{d}^2 f(r)}{\mathrm{d}r^2} + \frac{1}{r}\frac{\mathrm{d}f(r)}{\mathrm{d}r} - \left(\frac{4}{r^2} + \frac{3\Omega_0'}{r\Omega_0} + \frac{\Omega_0''}{\Omega_0}\right) f(r) = 0. \qquad (2.8)$$

In (2.6)–(2.8), the prime denotes a derivative with respect to the radial coordinate r. The function $f(r)$ characterizes the interaction of the strain field with the vortex. For large r, it satisfies $f(r) \sim r^2$ such that it matches the external strain field. Equation (2.8) was also given by Jiménez *et al.* (1996) and Eloy & Le Dizès (1999) in the case without axial flow. In the configuration of a Rankine vortex with an axial jet, an explicit expression for the function f can be derived, as shown in Lacaze *et al.* (2005).

As mentioned in §1, the elliptic instability can be interpreted as a process of resonance between linear modes of the underlying vortex (here the Batchelor vortex) with the correction induced by the strain field. In the next section, some of the properties of the inviscid normal modes of the Batchelor vortex are described. The conditions of resonance are considered in §3.1.

2.2. *Inviscid linear modes of the Batchelor vortex*

The velocity field $\boldsymbol{u}'$ and pressure field p' of linear normal mode perturbations are written in the form

$$(\boldsymbol{u}', p') = (\boldsymbol{u}_K(r), p_K(r)) \exp(\mathrm{i}kz + \mathrm{i}m\theta - \mathrm{i}\omega t), \qquad (2.9)$$

where ω is the temporal frequency and k and m are the axial and azimuthal wavenumbers, respectively. This expression inserted in the linearized Euler equations leads to a second-order differential equation for the pressure amplitude p_K (see Le Dizès 2004). The dispersion relation of the linear modes is obtained by enforcing on p_K adequate boundary conditions at the origin and at infinity.

For the Rankine vortex without axial flow, the dispersion relation has been known for a long time (see for instance Saffman 1992). In such a case, the linear modes are the so-called Kelvin modes first described by Kelvin (1880). For such a vortex, the Kelvin modes form a basis for perturbations confined within the vortex core
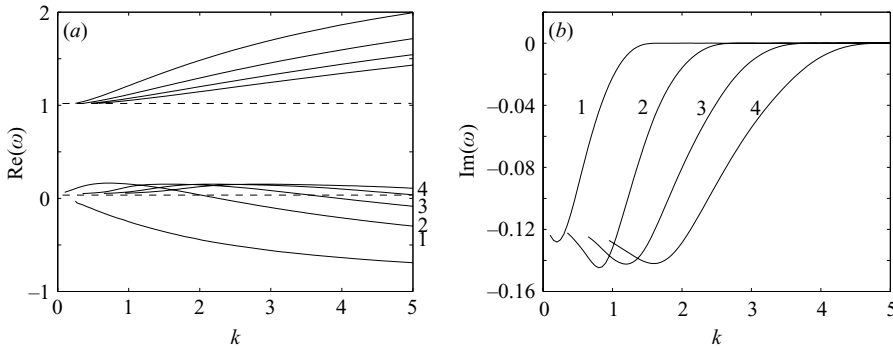
FIGURE 1. Dispersion relation for a Lamb–Oseen vortex ($W_0 = 0$). (*a*) Frequencies as a function of the axial wavenumber. Dotted lines delimit the frequency interval of the critical-layer modes. (*b*) Inviscid damping rate of critical-layer modes. Numbers in (*a*) and (*b*) indicate the label of the branches.

(Arendt, Fritts & Andreassen 1997), and hence all perturbations acting within the vortex core may be described in terms of Kelvin modes. In addition, for any fixed axial wavenumber k, and azimuthal wavenumber m, the set of frequencies is found to be discrete and within a fixed interval. In the case of a Rankine vortex with constant axial flow in the core, it has been shown that the Kelvin modes are slightly modified owing to the presence of the jet (Loiseleux, Chomaz & Huerre 1998). Except for small values of k, the jet acts mostly as a Doppler frequency shift.

The effect of a continuous profile on the characteristics of the modes is more complex (Sipp & Jacquin 2003; Le Dizès & Lacaze 2005; Fabre *et al.* 2006). For a Lamb–Oseen vortex (Batchelor vortex without axial flow), Sipp & Jacquin (2003) showed that linear inviscid normal modes become singular when their angular frequency is in the range of the angular velocity of the vortex. In such cases, the linear mode possesses a critical-layer singularity. This singularity can be smoothed by introducing viscous effects (Le Dizès 2004), but the mode is no longer neutral: it has a damping rate which becomes large when the critical-layer singularity is close to the vortex centre. An important point is that the damping rate does not depend on the Reynolds number for large Reynolds numbers. Moreover, the eigenfrequency can be computed by integrating the non-viscous equation in the complex plane above the singularity if $m > 0$ (below the singularity if $m < 0$) (see Sipp & Jacquin 2003, for details). Fabre *et al.* (2006) have shown good agreement between this procedure and results obtained from a fully viscous calculation. Figure 1 shows the dispersion relation of the modes $m = 1$ obtained for the Lamb–Oseen vortex by the contour deformation procedure. The branches are identified by a label l (l starts from 1 for the first retrograde mode). This label can be associated with the number of zeros of the eigenmode radial velocity profile in the radial direction (Sipp & Jacquin 2003). The frequency range where the eigenmodes possess a critical-layer singularity has been indicated in figure 1(*a*). The damping rate of the critical-layer modes is plotted in figure 1(*b*). It can be seen that the damping increases as the (real part of the) frequency of the mode increases in agreement with the displacement of the critical-layer singularity toward the vortex centre.

As long as axial flow is small, the picture of the temporal branches is not strongly modified (see also Le Dizès & Lacaze 2005). In figure 2, we present the frequencies of the modes $m = 1$ for the Batchelor vortex with $W_0 = 0.1$. We recover the same
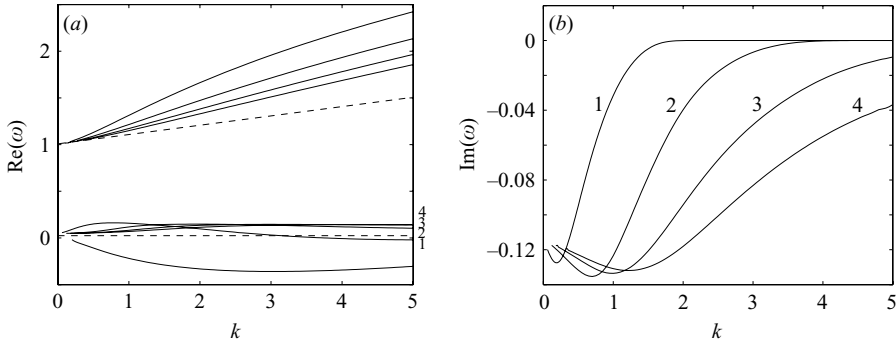
FIGURE 2. Same as figure 1, for $W_0 = 0.1$.

structure of the branches as for the Lamb–Oseen vortex, but a few differences can also be pointed out. The most important of these differences is the modification of the frequency range of critical-layer modes. In the presence of axial flow, the frequency range of critical-layer modes depends on the axial wavenumber. Axial flow has another important effect: it breaks the symmetry of the dispersion relation between the positive and negative azimuthal wavenumbers. We shall see in the next section that these two differences allow new linear mode resonances to occur.

3. Elliptic instability characteristics

In this section, the main steps of the theoretical analysis leading to the characterization of the elliptic instability in a Batchelor vortex are provided. The effect of axial flow on the resonant modes is first quantified. Then, its influence on the instability growth rate is computed and a complete instability diagram is obtained as a function of the axial flow parameter W_0.

3.1. *Characteristics of the principal modes*

The theory of the elliptic instability is based on an asymptotic analysis with respect to the strain rate ε, which is assumed small. The basic idea is presented in the work of Moore & Saffman (1975) and Tsai & Widnall (1976). For small ε, the mechanism of the elliptic instability can be understood as a phenomenon of resonance: the vortex which is axisymmetric at leading order possesses neutral (or almost neutral) normal modes that can be resonantly coupled with the $O(\varepsilon)$ correction induced by the external strain field. Upon remarking that this correction can be interpreted as a stationary ($\omega = 0$) axially homogeneous ($k = 0$) wave of azimuthal wavenumber $m = \pm 2$ (see terms proportional to ε in (2.6) and (2.7)), the condition of resonance of two normal modes 1 and 2 with this correction is easily written as:

$$\omega_2 = \omega_1, \quad k_2 = k_1, \quad m_2 = m_1 \pm 2. \tag{3.1}$$

The above condition is satisfied by numerous couples of normal modes. However, previous works on the Lamb–Oseen vortex (Eloy & Le Dizès 1999) and on the Rankine vortex (Eloy & Le Dizès 2001; Lacaze *et al.* 2005) have demonstrated that resonant configurations (satisfying (3.1)) corresponding to branches with the same label are, in general, the most unstable. We then focus on these resonant configurations, which are called 'principal modes' (Eloy & Le Dizès 2001).

Contrarily to the Rankine vortex (Lacaze *et al.* 2005), some inviscid normal modes are now damped by a critical-layer singularity and thus they should not *a priori* be
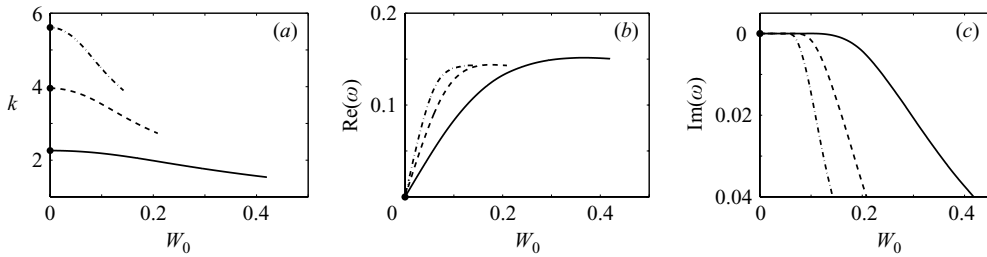
FIGURE 3. Characteristics of the first principal modes $(m_1, m_2) = (-1, 1)$ as a function of W_0. (a) Axial wavenumber k. (b) Frequency $\mathrm{Re}(\omega)$. (c) Critical-layer damping rate $\mathrm{Im}(\omega)$ of the resonant mode $m = 1$. Solid line, dashed line and dash-dot line correspond to the three first labels $l = 1, 2, 3$, respectively. Curves in (a) and (b) are ended when $\mathrm{Im}(\omega) < -0.04$ (see text).
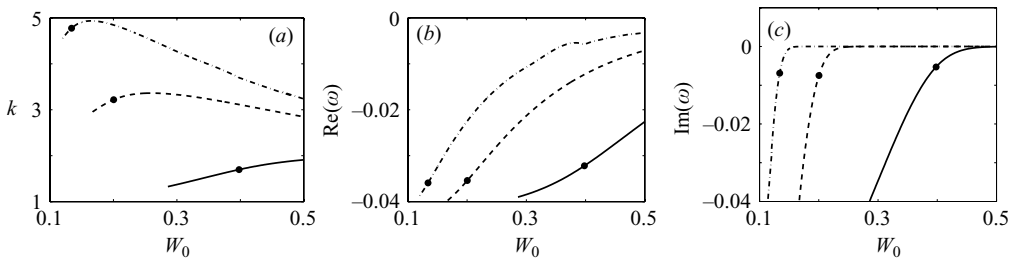

FIGURE 4. Characteristics of the first principal modes $(m_1, m_2) = (-2, 0)$ as a function of W_0. (a) Axial wavenumber k. (b) Frequency $\mathrm{Re}(\omega)$. (c): Critical layer damping rate $\mathrm{Im}(\omega)$ of the resonant mode $m = -2$. Solid line, dashed line and dash-dot line correspond to the three first labels $l = 1, 2, 3$, respectively. As in figure 3, curves in (a) and (b) are ended when $\mathrm{Im}(\omega) < -0.04$. The condition of perfect resonance (3.2) is indicated by a black circle.

involved in any resonance. However, if the damping is small, the growth induced by the coupling could still be larger. For this reason, we have chosen to monitor also the critical-layer modes and allow the resonance of these modes as long as their damping rate is $O(\varepsilon)$.

Figures 3(a) and 3(b) show the wavenumber and the frequency of the first principal modes of azimuthal wavenumbers $(m_1, m_2) = (-1, 1)$. For $W_0 = 0$, we can check that the results of Eloy & Le Dizès (1999) for the Lamb–Oseen vortex are recovered. In that case, all the principal modes $(-1, 1)$ are stationary ($\omega = 0$). When W_0 is non-zero, the frequency of the principal modes $(-1, 1)$ is not zero anymore. This is due to the symmetry breaking mentioned above between the modes $m = 1$ and $m = -1$. We have chosen to end the curves when one of the two resonant modes has a damping rate $\mathrm{Im}(\omega) < -0.04$. This value is arbitrary, but for the strain field we consider, we expect resonance not to lead to instability if one of the modes has a stronger damping rate. In figure 3(c), we show the dependence of this damping rate with respect to W_0. The other resonant mode ($m = -1$) remains always neutral.

Figures 4(a) and 4(b) show the characteristics of the principal modes $(-2, 0)$. It is worth mentioning that no resonance exist between such azimuthal modes without axial flow. This is due to the strong critical-layer damping of the mode $m = -2$ for $W_0 = 0$. The variation of the critical-layer damping rate is displayed in figure 4(c). We clearly see in this plot that an axial flow can sufficiently modify the spectrum, especially the frequency range where critical layers are present such that new resonant modes become possible. We remark again that in the case without axial flow, only

the resonance $(m_1, m_2) = (-1, 1)$ could arise. As the axial parameter is increased, the resonance $(-1, 1)$ progressively disappears and is replaced by other resonances: $(-2, 0)$, then $(-3, -1)$, $(-4, -2)$, as will be shown below. Each principal mode exists in finite intervals of W_0 in which the two resonant modes do not possess critical layers or in which one of the modes is neutral and the other one is only slightly damped by a critical layer. Only very few principal modes are possible. Note in particular that there are no principal modes $(m, m + 2)$ with $m \geqslant 0$ for positive axial flow. In the frequency range where branch crossing could have been possible, one of the two modes is indeed always strongly damped by a critical-layer singularity.

In figures 3(a) and 4(a), a small black disk on each curve indicates the wavenumber of the principal mode for which

$$\omega - kW_0 = \frac{m_1 + m_2}{2}. \tag{3.2}$$

This condition corresponds to the condition of perfect resonance mentioned in Eloy & Le Dizès (2001) and Lacaze *et al.* (2005). As shown in Waleffe (1990) and Le Dizès (2000b), when this condition is satisfied, the resonant modes can be expressed near the vortex centre as the most unstable local plane waves for which a local estimate of the growth rate is $(9/16)\varepsilon_0$ (ε_0 being the strain rate in the vortex centre). Eloy & Le Dizès (2001) and Lacaze *et al.* (2005) have also shown that the instability is maximized when this condition is satisfied and that the local growth rate is a fairly good estimate for the elliptic instability growth rate in the inviscid limit. We shall see below that this condition is also useful when selecting the most unstable configurations in the present case.

3.2. *Growth rate of the instability*

The growth rate of the resonant Kelvin modes can be computed by a multi-scale analysis, as shown in Moore & Saffman (1975). The velocity–pressure perturbation $U' = (u', p')$ is represented as a sum of two resonant modes of amplitude A_1 and A_2

$$U = A_1(\varepsilon t)U_{K_1}(r) \exp(\mathrm{i}k_1 z + \mathrm{i}m_1\theta - \mathrm{i}\omega_1 t) + A_2(\varepsilon t)U_{K_2}(r) \exp(\mathrm{i}k_2 z + \mathrm{i}m_2\theta - \mathrm{i}\omega_2 t), \tag{3.3}$$

where the wavenumbers and frequency of the two modes satisfy (3.1). From the equations at order ε, two equations for A_1 and A_2 are obtained as orthogonality conditions. These equations possess solutions of the form

$$A_1(\varepsilon t) = B_1 e^{\sigma \varepsilon t}; \quad A_2(\varepsilon t) = B_2 e^{\sigma \varepsilon t}, \tag{3.4}$$

which defines the normalized complex growth rate σ. Its real part $\mathrm{Re}(\sigma)$ is what is usually called the growth rate, whereas its imaginary part $\mathrm{Im}(\sigma)$ corresponds to a frequency detuning. The complex growth rate σ is found to satisfy a relation which is written as (see Eloy & Le Dizès 1999, 2001 for details)

$$\left(\sigma \mathscr{I}_{11} + \mathrm{i}k_\varepsilon \mathscr{Q}_{11} - \frac{1}{\varepsilon Re}\mathscr{L}_{11} - \frac{\mathrm{Im}(\omega)}{\varepsilon}\mathscr{I}_{11}\right) \times \left(\sigma \mathscr{I}_{22} + \mathrm{i}k_\varepsilon \mathscr{Q}_{22} - \frac{1}{\varepsilon Re}\mathscr{L}_{22}\right) = \bar{\mathscr{N}}_{12}\mathscr{N}_{21}, \tag{3.5}$$

where

$$\mathscr{X}_{\alpha\beta} = \left\langle U_{K_\alpha}^A, \mathscr{X}U_{K_\beta}\right\rangle,$$

and $U_{K_\alpha}^A$ is the velocity–pressure amplitude of the adjoint Kelvin mode, solution of the adjoint operator obtained with the scalar product ($\bar{X}$ denotes the complex conjugate
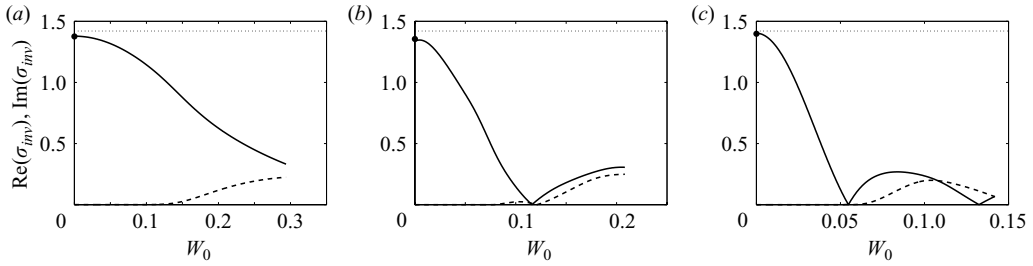
FIGURE 5. Characteristics of the first principal modes $(-1, 1, l)$. Inviscid complex growth rate σ_{inv} (see (3.6)) as a function of W_0. Solid line, $\mathrm{Re}(\sigma_{inv})$ (growth rate); dashed line $\mathrm{Im}(\sigma_{inv})$ (frequency detuning); Dotted line: local maximum growth rate. The label l of the principal modes varies from 1 to 3 from left to right. The condition of perfect resonance (3.2) is indicated by a black circle.
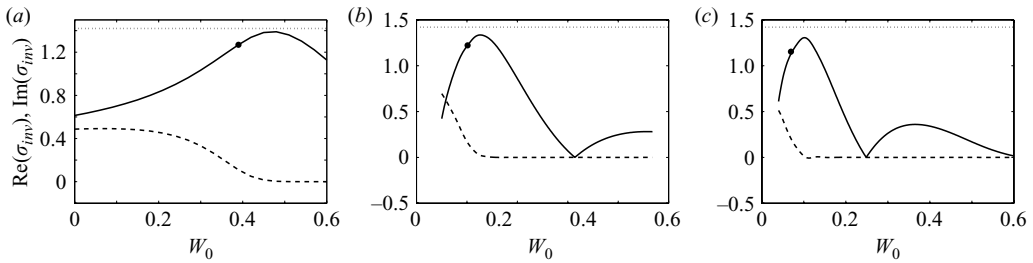

FIGURE 6. Same as figure 5 but the for the principal modes $(-2, 0, l)$.

of X):

$$\langle X, Y \rangle = \int_0^\infty (\bar{X} \cdot Y) r \, \mathrm{d}r.$$

The term $\mathscr{J}_{\alpha\alpha}$ in (3.5) represents the energy of the mode α, $\mathscr{N}_{\alpha\beta}$ measures the coupling between the two modes and the strain field. The term $\mathscr{Q}_{\alpha\alpha}$ permits us to take into account a small wavenumber detuning with respect to exact resonance ($k_1 = k_2 = k_0 + \varepsilon k_\varepsilon + O(\varepsilon^2)$ where k_0 corresponds to the value plotted in figures 3(a) or 4(a)). The term $\mathrm{Im}(\omega)\mathscr{J}_{11}/\varepsilon$ is the damping term due to the critical layer (for which we implicitly assume $\mathrm{Im}(\omega) = O(\varepsilon)$). The viscous damping of each mode, given by the term $(1/\varepsilon Re)\mathscr{L}_{\alpha\alpha}$, has also been included in (3.5) in order to cut off small wavelengths. Including viscous effects on the perturbation is not in contradiction with our assumption of inviscid base flow. The viscous damping of large-wavenumber Kelvin modes is indeed proportional to k^2/Re, and thus on a faster scale than the viscous time scale of the base flow if k is large. For example, if $k = O(\varepsilon^{-1/4})$ and $Re = O(\varepsilon^{-3/2})$, the viscous time scale of the perturbation is $O(\varepsilon^{-1})$ as the elliptic instability time scale, whereas the viscous diffusion time scale of the base flow is $O(\varepsilon^{-3/2})$.

If no damping term is taken into account, we obtain a simple inviscid estimate

$$\sigma_{inv} = \left(\frac{\bar{\mathscr{N}}_{12}\mathscr{N}_{21}}{\mathscr{J}_{11}\mathscr{J}_{22}} \right)^{1/2}. \tag{3.6}$$

This expression is plotted for the first three principal modes $(-1, 1, l)$ and $(-2, 0, l)$ in, figures 5 and 6, respectively. As in figures 3 and 4, the curves have been ended when the critical-layer damping of one of the two modes has become too important.
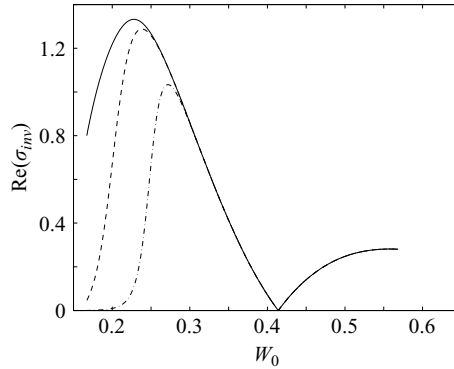
FIGURE 7. Maximum (normalized) inviscid growth rate including the critical-layer damping for the principal mode $(-2, 0, 2)$. Solid line limit for large ε (i.e. expression (3.6)); dashed line, $\varepsilon = 0.01$; dot-dashed line $\varepsilon = 0.0001$.

In these plots a small black disk indicates the growth rate for the parameter satisfying the condition (3.2) of perfect resonance, as indicated in figures 3(*a*) and 4(*a*). For the principal modes $(-1, 1)$, the condition of perfect resonance is obtained for $W_0 = 0$. It corresponds exactly to the axial flow value which maximizes the instability. The maximum growth rate is also predicted well by the local maximum growth rate estimate $(9/16)\varepsilon_0/\varepsilon \approx 1.42$.

For the principal modes $(-2, 0, l)$, the perfect resonance growth rate is also close to the maximum growth rate and to the local maximum growth rate estimate. As for the case of the Rankine vortex (Lacaze *et al.* 2005), the condition of perfect resonance thus provides a good prediction of the parameters which maximize the instability. The inviscid complex growth rate plotted in figures 5 and 6 does not take into account the 'inviscid' damping associated with the critical layer. When this damping term is considered, the inviscid growth rate becomes dependent on the value of ε. This dependency is illustrated for the principal mode $(-2, 0, 2)$ for two values of ε in figure 7. One can check that the smaller the value of ε, the stronger the effect of the critical-layer damping.

When the axial wavenumber detuning is considered, the growth rate of each principal mode becomes peaked in the (W_0, k)-plane near the parameter of perfect resonance. Typically, one obtains growth rate contours of the form illustrated in figure 8. The curve $k = k_0(W_0)$, as plotted in figure 4(*a*) for the principal modes $(-2, 0, l)$, is displayed as a solid line. The growth rate contours are not symmetric with respect to this curve. This is due to the critical-layer damping which is more important on one side of this curve. The-leading-order variation of the (normalized) critical-layer damping with respect to k_ε is given for mode 1 by

$$\sigma_{CL}(k_\varepsilon) = \mathrm{Im}\left(\frac{\mathcal{D}_{11}}{\mathcal{I}_{11}}\right) k_\varepsilon + \frac{\mathrm{Im}(\omega)}{\varepsilon}. \quad (3.7)$$

The dashed line in figure 8 indicates the axial wavenumber $k = k_0 + \varepsilon k_\varepsilon$ for which the critical-layer damping approximated by (3.7) vanishes. Above this curve, (3.7) provides non-physical positive values for σ_{CL} which have been replaced by zero in the general equation (3.5) for the growth rate. In figure 8, the vertical line, which sharply cuts the growth rate contour, delimits the region of existence of the principal mode. On this line, the branches $\omega(k)$ of the two Kelvin modes forming the principal
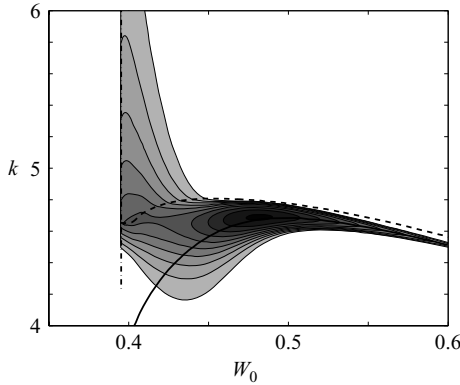
FIGURE 8. Illustration of the growth rate contours in the (W_0, k)-plane of a principal mode for fixed Reynolds number and ε. Here the principal mode $(-4, -2, 1)$ for $Re = 20\,000$ and $\varepsilon = 0.015$. The curve of exact resonance $k = k_0(W_0)$ is indicated by a solid line. The dashed line limits the region where the critical-layer damping is present in (3.5). The dash-dotted vertical line limits the region of existence of the principal mode.
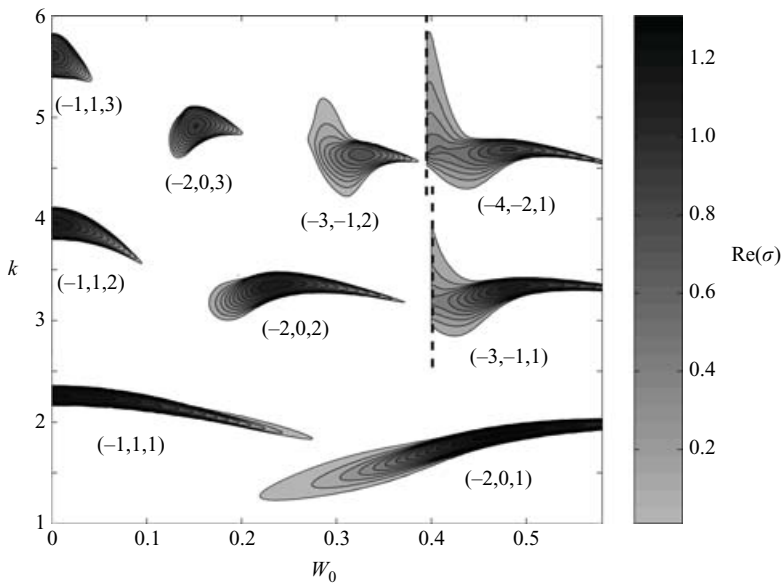

FIGURE 9. Instability area of the principal coupling modes in a plane (W_0, k) for $Re = 20\,000$ and $\varepsilon = 0.01$. Grey levels correspond to the intensity of the growth rate.

mode are tangent with each other at the resonant point k_0. On the left of this line, the two branches $\omega(k)$ do not cross anymore and the principal mode does not exist. The growth rate expression, (3.5), is not expected to apply near this line as higher-order terms should be included to capture this topological change.

Contour plots such as that shown in figure 8 can be computed for each principal mode. When these plots are superimposed in the (W_0, k)-plane, we obtain a multitude of instability 'islands' associated with each principal mode. In figures 9, 10 and 11, such instability diagrams are given for three couples of parameters (Re, ε). Each 'island' corresponds to a principal mode. We immediately see that numerous instability
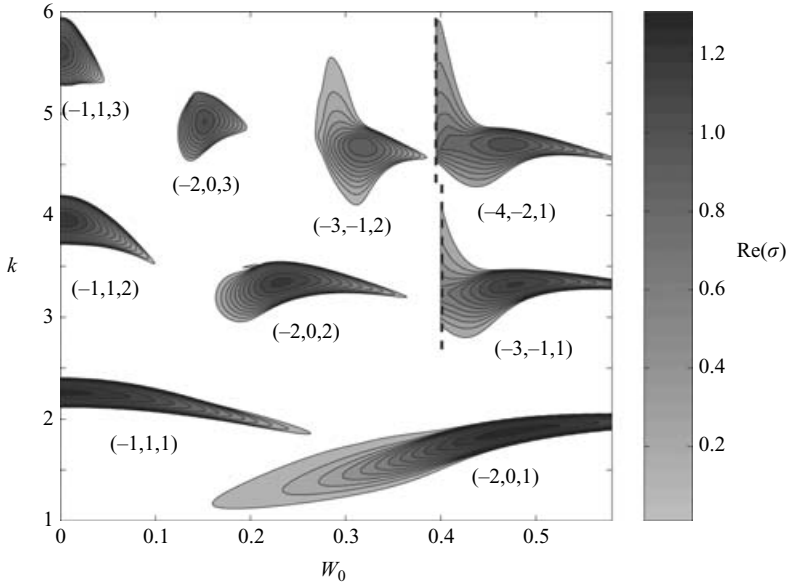
FIGURE 10. Same as figure 9 but for $\varepsilon = 0.015$.
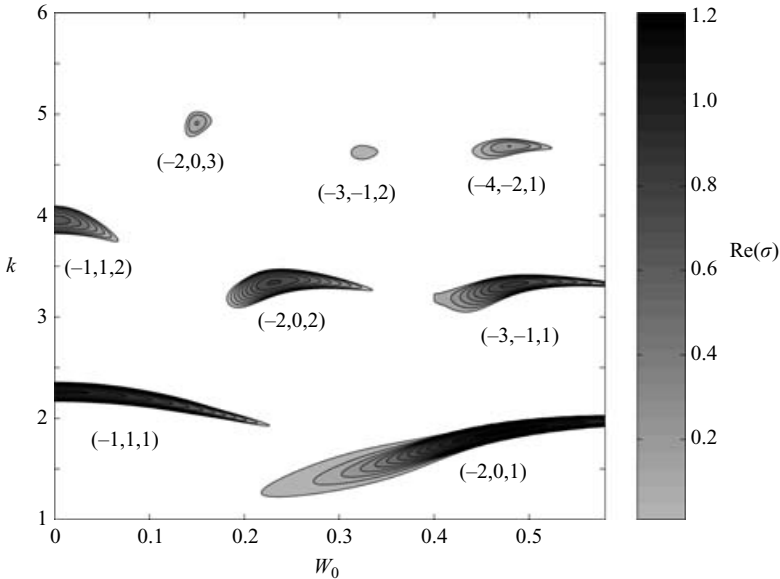
FIGURE 11. Same as figure 9 but for $Re = 5000$ and $\varepsilon = 0.01$.

modes are possible, each in a different region of the parameter space. In particular, the principal modes $(-1, 1, l)$ are seen no longer to be the only possible unstable modes in the presence of axial flow. The other principal modes $(-2, 0, l)$, $(-3, -1, l)$, etc, characterized by a more complex spatial structure become possible unstable modes as W_0 is progressively increased. The variations of the growth rate for two fixed values of the axial flow ($W_0 = 0.25$; $W_0 = 0.48$) will be compared to results obtained by numerical simulations in the next section.
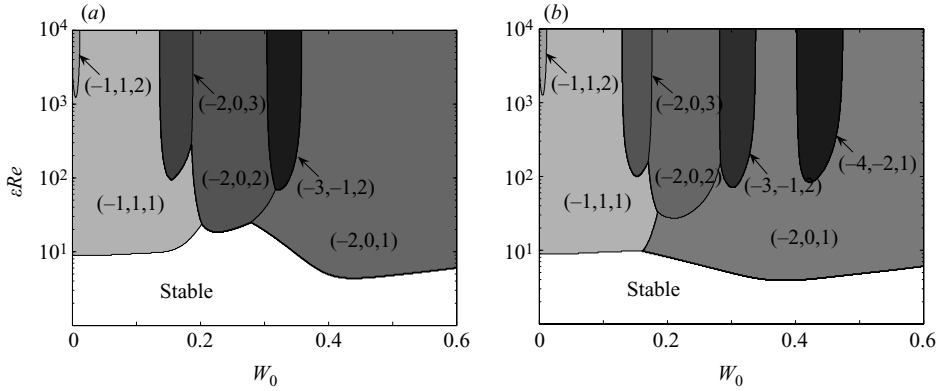
FIGURE 12. Most unstable principal mode in the $(W_0, \varepsilon Re)$-plane for (a) $\varepsilon = 0.01$ and (b) $\varepsilon = 0.1$.

By comparing the figures 9, 10 and 11 with each other, we immediately see that the different instability regions spread as either ε or Re is increased, as expected. The variation with respect to the Reynolds number is also visible in figure 12. In these figures, the characteristics of the most unstable principal modes are displayed in the parameter plane $(W_0, \varepsilon Re)$ for two values of ε.

4. Numerical results and comparison

In this section, the theoretical results are compared to numerical results obtained for a pair of counter-rotating vortices with an axial jet. A similar comparison has been performed for vortex pairs without axial flow in Le Dizès & Laporte (2002).

4.1. *Numerical procedure*

The numerical computation is performed in two steps. The basic flow is first obtained, then the most unstable linear mode is computed.

The basic flow is obtained by a two-dimensional numerical simulation. The simulation is initialized with two counter-rotating Gaussian vortices without axial flow of core radius R_0, circulation Γ, and separated by a distance b. This initial condition does not form a solution to the Euler equations. Thus, there is first a rapid relaxation phase during which the vortices equilibrate with each other (Sipp *et al.* 2000). Then, the quasi-steady state is obtained after the relaxation process is advected at a constant speed and slowly evolves owing to viscous diffusion. In the simulation, the self-advection speed of the vortex pair is subtracted such that the vortices remain in the computational domain. The properties of the quasi-steady state have been analysed in Sipp *et al.* (2000) and Le Dizès & Verga (2002). For the ratios of R_0/b that we use, it has been shown that each vortex can be considered as a Gaussian vortex in equilibrium with the external strain field generated by the other vortex. Moreover, the strain rate of the external field has been shown to be close to the value $\varepsilon = \Gamma/(2\pi b^2)$ obtained by a point-vortex approximation. The two-dimensional simulation is stopped after the relaxation process. The vortex radius R has slightly increased owing to viscous diffusion and it is this new value which is considered for length-scale normalization. The normalized strain rate parameter ε is therefore defined by

$$\varepsilon = \frac{R^2}{b^2}. \tag{4.1}$$

The two-dimensional evolution of the axial flow is completely decoupled from the dynamics of the other velocity components and can be treated separately. It satisfies the same advection–diffusion equation as the axial vorticity. Thus, if we consider an axial flow velocity field proportional to the axial vorticity, we automatically form a solution. However, for such a solution, the axial flow is in the opposite direction when comparing either vortex with the other. Because, in most applications, vortices possess axial flow in the same direction, we have also integrated the advection–diffusion equation with an initial condition defined by $W(t=0) = |\omega_z(t=0)|$. For the values of R_0/b we have considered, the solution was also found to follow closely the evolution of $|\omega_z|$ in both vortices in that case. After the relaxation process, the strength of the axial flow was adjusted such that $W = (W_0/2)|\omega_z|$ in each vortex core, in agreement with (2.4) and (2.5).

To compute the most unstable linear mode, the Navier–Stokes equations are linearized with respect to the frozen basic state. Perturbations are chosen with a fixed axial wavelength $\lambda = 2\pi/k$. The perturbation equations are integrated forward in time starting from a random perturbation field. When the basic flow is unstable, the perturbation quickly becomes a combination of growing modes. The most unstable mode characteristics are extracted by integrating the perturbation equations for a sufficiently long time (typically 30 to 100 times the inverse growth rate).

For each set of parameters (Re, W_0, R/b and k), we obtain the frequency, the growth rate and the spatial structure of the most unstable mode which can be compared to the theory.

4.2. *Numerical code*

The two-dimensional equations and the three-dimensional linearized equations are solved using a high-order spectral-element method. The numerical code has previously been applied successfully to several problems (see for instance Ryan, Thompson & Hourigan 2005; Thompson *et al.* 2001*a*, *b*).

The time integration uses a three-step time-splitting method and achieves second-order time accuracy, and is described in Karniadakis, Israeli & Orszag (1991). The spatial accuracy was determined at run time by choosing the order of the tensor-product of interpolating polynomials within each macro-element as is usually possible with finite-element schemes. In all the simulations quoted herein, 700 macro-elements were employed with eighth-order polynomial interpolants. A square domain was considered with a domain length and width of 40 vortex diameters.

The accuracy of the code was validated by comparing the damping rate of the strain rate oscillation during the two-dimensional relaxation process with the analytical prediction (Le Dizès & Verga 2002). A maximum deviation of 0.025 % was noted when eighth-order polynomial interpolants were used.

4.3. *Results and comparison*

In all the numerical investigations, the Reynolds number and the normalized vortex separation distance were held fixed, $Re = 3180$; $R/b = 0.25$. This corresponded to an external strain rate $\varepsilon = 0.0625$. This relatively high strain rate was chosen to increase the growth rate of the three-dimensional instabilities (and hence decrease computational expense) while maintaining a sufficiently low strain rate that valid comparisons could be made with the analytical theory.

Several values of W_0 were investigated. For each value of W_0, 120 wavenumbers equally spaced in the range $k = 1$ to 6 were examined, and the findings were compared with analytical theory. Only two values of W_0 are detailed in this paper; however,
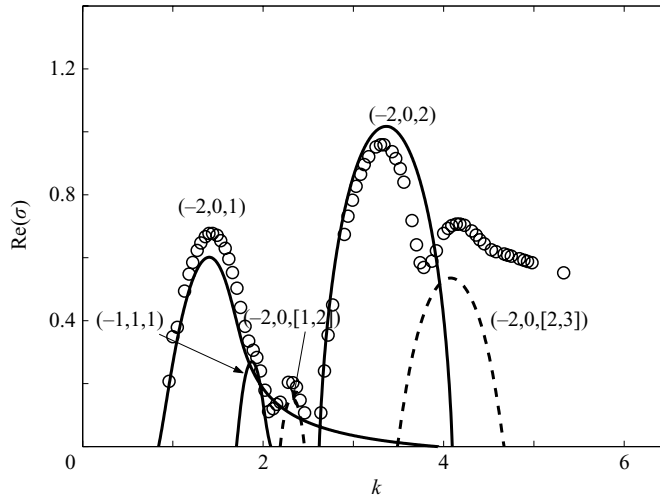
FIGURE 13. Growth rate of the elliptic instability as a function of the axial wavenumber for $W_0 = 0.2494$, $Re = 3180$ and $\varepsilon = 0.063$. Symbols are numerical results for counter-rotating vortices with axial flow in the same direction. Solid curves and dashed curves are theoretical predictions for principal and non-principal modes, respectively (see text for explanation on the labels).

it should be stressed that the excellent agreement between analytical and numerical findings described herein is typical for all investigations performed in this study.

Figure 13 shows a comparison between the analytical and numerical investigations for $W_0 = 0.2494$. Here, two main principal modes are noted in both investigations. The first, with a peak growth rate at $k \simeq 1.4$, corresponds to the principal mode $(-2, 0, 1)$. The second mode has a peak growth rate at $k \simeq 3.4$, and corresponds to the principal mode $(-2, 0, 2)$. The theory also predicts that the principal mode $(-1, 1, 1)$ is unstable near $k \simeq 1.9$. The growth rate of this mode is, however, smaller than the growth rate of the principal mode $(-2, 0, 1)$ for almost all wavenumbers. This mode is visible on the numerical results only very close to $k \simeq 1.92$. The principal mode $(-1, 1, 1)$ was the most unstable mode in the configuration without axial flow. Although this mode is still unstable for $W_0 = 0.2494$, it is now superseded by several other modes. It is therefore not expected to be observed experimentally.

Two further modes are noted in the numerical computation close to $k \simeq 2.3$ and $k \simeq 4.1$. These modes are not associated with any theoretical principal mode. However, both possess a spatial structure involving azimuthal wavenumbers $m = -2$ and $m = 0$. Going back to the theory, we noted that these modes could be associated with the resonance of Kelvin modes from branches of different labels. Using the same technique as above, we computed the growth rate associated with the two non-principal modes $(-2, 0, [1, 2])$ and $(-2, 0, [2, 3])$. In the notation $(-2, 0, [2, 3])$, the first two indexes denote the azimuthal wavenumbers of the resonant Kelvin modes, and the last two denote the branch labels of each mode. The theoretical growth rate of these modes is indicated in dashed lines in figure 13. Although slightly below the numerical growth rate, the agreement is remarkable.

Figure 14 shows a comparison between the analytical and numerical investigations for $W_0 = 0.482$. Considering figure 14, we observe that this is a region of the parameter space which has several modes which are unstable, the dominant mode in this region being mode $(-2, 0, 1)$. Three principal modes are observed both numerically and
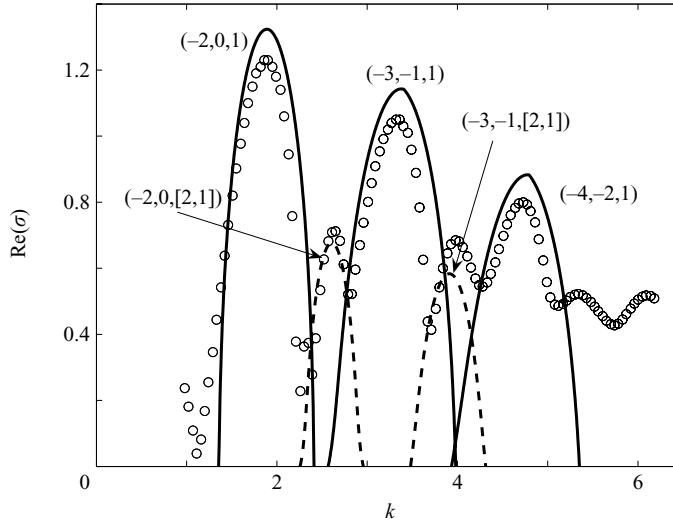
FIGURE 14. Same as figure 13 but for $W_0 = 0.482$.

analytically in the figure, further to this, several modes of lower maximum growth rate are also observed. In each case, the analytical work and the numerical simulations are in close agreement. The three principal modes observed correspond to the Kelvin mode couplings $(-2, 0, 1)$, $(-3, -1, 1)$ and $(-4, -2, 1)$. Two non-principal modes are also observed both numerically and analytically. Their presence was noted only after the numerical simulations; subsequently, analytical work successfully determined the growth rates for these mode couplings. Further modes are noted from the numerical simulations at high wavenumbers; however, the maximum growth rate observed for these is very small when compared to the other modes identified.

It is worth mentioning that although unstable non-principal modes have been observed for both axial flow parameters, they have always been found to be less unstable than principal modes. It is therefore very unlikely that they would be observed experimentally. This provides an *a posteriori* justification for not having considered all these modes in the theory.

Figure 15 shows contours of the perturbation vorticity fields for each of the modes identified for $W_0 = 0.482$. The images are taken in a two-dimensional horizontal cross-section which is at an arbitrary axial position. In each case, the perturbation field for both vortex cores are shown. The figures are taken at a given instant in time, after the perturbation field was allowed to grow sufficiently, such that the mode structures are clearly visible. The images are typical of the perturbation vortex structures at any time once the perturbation fields are developed. It may be observed that, in each case, one of the vortices has a stronger perturbation field than the other. This is due to the perturbation field growing from random noise. Although both vortices exhibit the same growth rate, the perturbation field in one emanates from a random field which is more predisposed to the mode growth than the other. It is through these images that the azimuthal structure of modes may be identified from the numerical simulations. For the three principal modes identified $(-2, 0, 1)$, $(-3, -1, 1)$ and $(-4, -2, 1)$, not only does the growth rate agree closely with the analytical findings, the perturbation flow field agrees entirely with the predictions, given the mode type associated with each peak. The azimuthal wavenumbers $m = -2$ and $m = -3$ are also clearly visible
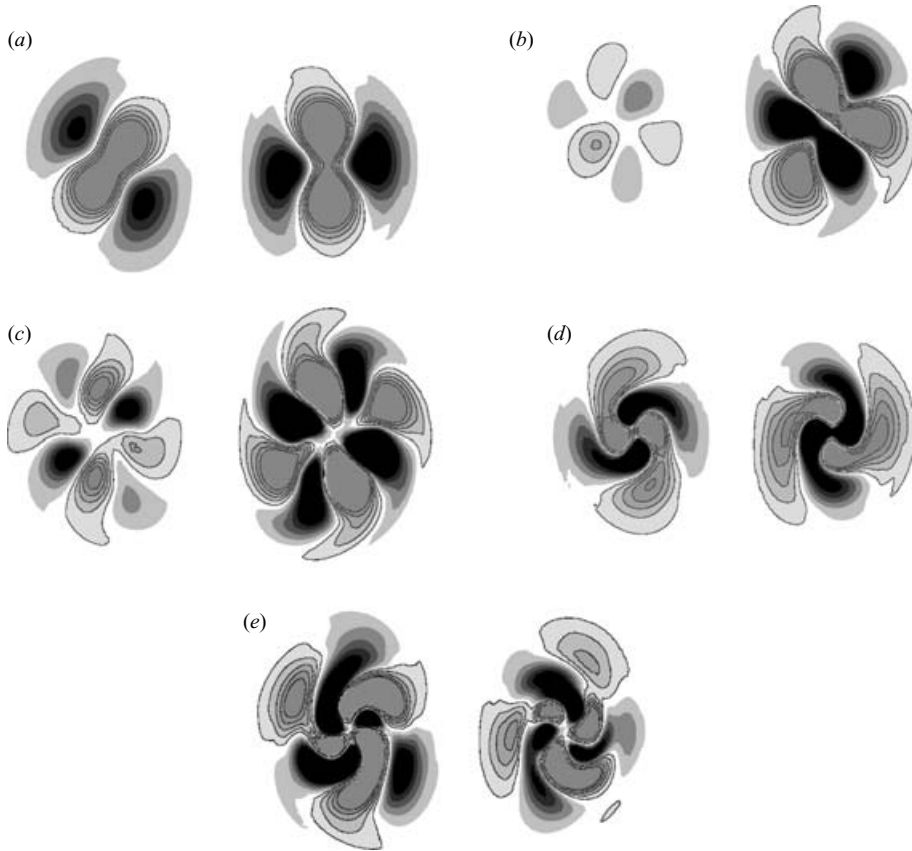
FIGURE 15. Numerical results for the perturbation vorticity fields for each identified mode shown in figure 14. $W_0 = 0.482$, $Re = 3\,180$ and $\varepsilon = 0.063$. (*a*) Mode $(-2, 0, 1)$, $k = 1.88$; (*b*) mode $(-3, -1, 1)$, $k = 3.23$; (*c*) mode $(-4, -2, 1)$, $k = 4.57$; (*d*) mode $(-2, 0, [2, 1])$, $k = 2.6$; (*e*) mode $(-3, -1, [2, 1])$, $k = 3.85$.

on the vorticity fields of the modes $(-2, 0, [2, 1])$ and $(-3, -1, [2, 1])$ shown in figures 15(*d*) and 15(*e*), respectively.

The addition of the axial velocity allows a temporal frequency ω to be observed which may be compared to the analytical prediction (see §3). An illustration of the temporal dynamics is shown in figure 16 for mode $(-2, 0, 1)$. In this case, the perturbation vortex cores are observed to twist about the axis of the base vortex core. As we are observing the perturbation vortex structure only on one plane along the axis, the perturbation vortex structures appear to rotate over time. It is apparent that there are two positive and two negative perturbation vortex structures for each base vortex. This is clear evidence of an $m = -2$ component in the perturbation. These structures appear to change subtly in size throughout the cycle. This is evidence of the $m = 0$ component. The frequencies of all the unstable modes considered for $W_0 = 0.482$ are presented in table 1. They are also compared to the analytical estimates which provides further confirmation that the modes observed numerically are identical to those predicted by the theory.

The small discrepancies observed between the numerical and analytical results can be attributed to a few factors which it is useful to recall. First, the theoretical
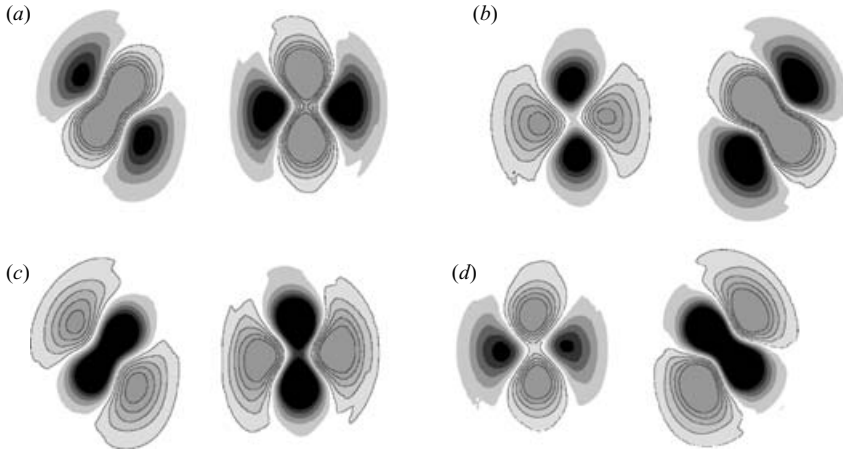
FIGURE 16. Snapshots of perturbation vorticity over a cycle ω. Each image is one eighth of a cycle from the previous one. The positive and negative vortices are observed to rotate about the axis of each base vortex. In this case, the mode is $(-2, 0, 1)$, $W_0 = 0.482$, $Re = 3\,180$, and $\varepsilon = 0.063$.

Mode	k	σ_{Th}	σ_{Num}	ω_{Th}	ω_{Num}
$(-2, 0, 1)$	1.88	1.32	1.23	-0.25	-0.26
$(-3, -1, 1)$	3.23	1.11	1.05	-0.61	-0.58
$(-4, -2, 1)$	4.57	0.83	0.8	-0.95	-1.04
$(-2, 0, [2, 1])$	2.6	0.68	0.71	-0.21	-0.22
$(-3, -1, [2, 1])$	3.85	0.57	0.69	-0.57	-0.60

TABLE 1. A comparison of results for the modes identified for $W_0 = 0.482$, $Re = 3180$ and $\varepsilon = 0.063$. The wavenumber is normalized by $1/R$, the growth rates σ_{Th} and σ_{Num} by $\Gamma/(2\pi b^2)$ and the frequencies ω_{Th} and ω_{Num} by $\Gamma/(2\pi R^2)$.

results were obtained by computing a leading-order viscous correction to inviscid predictions. Higher-order corrections may be significant for the low Reynolds number we considered in the numerics. Secondly, the two vortices were placed close to each other ($R/b = 0.25$). The strain rate induced by one vortex on the other was therefore important. Higher-order corrections in the strain rate could therefore affect both the theoretical description of the base flow and the calculation of the instability growth rate. Moreover, in most simulations, we have considered counter-rotating vortices with axial flow in the same direction. For this configuration, vorticity and axial flow are proportional to each other in the vortex cores, as in the theory, but in the region between the vortices, this is not the case: axial flow contributions add up, whereas vorticity contributions annihilate. This could affect the less localized modes in the vortex cores. Finally, before their destabilization, the two vortices are not only elliptically deformed, but also exhibit azimuthal deformations of higher order (see for instance Ehrenstein & Le Dizès 2005). Such deformations have not been taken into account in the theory. They may generate other instabilities (see Eloy *et al.* 2003), but they may also affect some of the present resonances.

It is worth mentioning that the discrepancies are not all in the same direction (see figure 13). This indicates that the above factors can be either stabilizing or destabilizing, and their contributions vary from one mode to the other.

5. Conclusion

In this paper, we have analysed the stability of a strained Batchelor vortex with respect to the elliptic instability. Only small axial flow parameters have been considered, for which the Batchelor vortex is stable with respect to inviscid perturbations. We have shown that axial flow modifies the characteristics of the elliptic instability. Without axial flow, the elliptic instability mode is formed of two stationary symmetric Kelvin modes $m = 1$ and $m = -1$. Axial flow breaks the symmetry between the Kelvin modes $m = 1$ and $m = -1$ such that the elliptic instability is no longer a sinuous stationary deformation in the presence of a small axial flow. For larger axial flow, the resonance between Kelvin modes $m = 1$ and $m = -1$ disappears because one of the two modes becomes strongly damped owing to a critical-layer singularity. However, another resonance between $m = 0$ and $m = -2$ becomes possible, leading to a new instability mode. As the axial flow is progressively increased, this resonance is replaced by another between modes $m = -1$ and $m = -3$ and so on. Complete instability diagrams associated with the principal modes have been obtained as functions of the axial flow parameter and the axial wavenumber for several values of the strain rate and the Reynolds number.

The theoretical results have been validated by a linear simulation of the instabilities developing in a pair of counter-rotating Batchelor vortices. In this system of vortices, each vortex is subject to the strain field induced by the other vortex. For each axial flow parameter, the normalized axial wavenumber of the perturbation has been varied between $kR = 1$ to 6. The characteristic features (spatial shape, growth rate, frequency) of the most unstable modes predicted by the theory have been recovered with good agreement. Other less unstable modes have also been observed in the simulation. They have been successfully attributed to resonance of non-principal modes associated with branches of different labels. Their theoretical growth rate has also been calculated and shown to compare favourably with the numerics.

Counter-rotating vortices are often used to describe the vortex system in the far wake behind an aircraft. Axial flow is still present in these vortices and can reach in certain cases more than 10 % the maximal azimuthal velocity. A principal instability mode $(-2, 0)$ could therefore be present. A pair of counter-rotating vortices is also known to be subject to the Crow instability. This long-wavelength instability is not expected to be affected by weak axial flow. However, it would be interesting to determine whether its nonlinear development could be modified by the elliptic instability mode $(-2, 0)$.

In the near wake behind an aircraft, axial flow is expected to be more important, but the strain field acting on a given vortex is usually rotating. In that case, the theory is slightly different as the rotation of the strain field has to be taken into account in the conditions of resonance (see Le Dizès & Laporte 2002). However, this rotation is always small so the main results of the present analysis are not expected to be modified: the sinuous instability mode $(-1, 1)$ is expected to be superseded by other resonant modes $(-2, 0)$, $(-3, -1)$, etc. as axial flow increases. How these new modes modify the merging process of co-rotating vortices is one of the questions which it is now important to address.

REFERENCES

ARENDT, S., FRITTS, D. C. & ANDREASSEN, O. 1997 The initial value problem for Kelvin vortex waves. *J. Fluid Mech.* **344**, 181–212.

ASH, R. L. & KHORRAMI, M. R. 1995 Vortex stability. In *Fluid Vortices* (ed. S. I. Green), chap. 8, pp. 317–372. Kluwer.

BATCHELOR, G. K. 1964 Axial flow in trailing line vortices. *J. Fluid Mech.* **20**, 645–658.

BAYLY, B. J. 1986 Three-dimensional instability of elliptical flow. *Phys. Rev. Lett.* **57**, 2160–2163.

BAYLY, B. J., ORSZAG, S. A. & HERBERT, T. 1988 Instability mechanisms in shear-flow transition. *Annu. Rev. Fluid Mech.* **20**, 359–391.

EHRENSTEIN, U. & LE DIZÈS, S. 2005 Relationship between co-rotating vortex-pair equilibria and a single vortex in an external deformation field. *Phys. Fluids* **17** (074103).

ELOY, C. & LE DIZÈS, S. 1999 Three-dimensional instability of Burgers and Lamb–Oseen vortices in a strain field. *J. Fluid Mech.* **378**, 145–166.

ELOY, C. & LE DIZÈS, S. 2001 Stability of the Rankine vortex in a multipolar strain field. *Phys. Fluids* **13** (3), 660–676.

ELOY, C., LE GAL, P. & LE DIZÈS, S. 2003 Elliptic and triangular instabilities in rotating cylinders. *J. Fluid Mech.* **476**, 357–388.

FABRE, D. & JACQUIN, L. 2004a Short-wave cooperative instabilities in representative aircraft vortices. *Phys. Fluids* **16**, 1366–1378.

FABRE, D. & JACQUIN, L. 2004b Viscous instabilities in trailing vortices at large swirl numbers. *J. Fluid Mech.* **500**, 239–262.

FABRE, D., SIPP, D. & JACQUIN, L. 2006 The Kelvin waves and the singular modes of the Lamb–Oseen vortex. *J. Fluid Mech.* **551**, 235–274.

HEATON, C. 2007 Centre modes in inviscid swirling flows, and their application to the stability of the Batchelor vortex. *J. Fluid Mech.* **576**, 325–348.

JIMÉNEZ, J., MOFFATT, H. K. & VASCO, C. 1996 The structure of the vortices in freely decaying two-dimensional turbulence. *J. Fluid Mech.* **313**, 209–222.

KARNIADAKIS, G. E., ISRAELI, M. & ORSZAG, S. A. 1991 High-order splitting methods of the incompressible Navier–Stokes equations. *J. Comput. Phys.* **97**, 414–443.

KELVIN, LORD. 1880 Vibrations of a columnar vortex. *Phil. Mag.* **10**, 155–168.

KERSWELL, R. R. 2002 Elliptical instability. *Annu. Rev. Fluid Mech.* **34**, 83–113.

LACAZE, L., BIRBAUD, A.-L. & LE DIZÈS, S. 2005 Elliptic instability in a Rankine vortex with axial flow. *Phys. Fluids* **17** (017101).

LE DIZÈS, S. 2000a Non-axisymmetric vortices in two-dimensional flows. *J. Fluid Mech.* **406**, 175–198.

LE DIZÈS, S. 2000b Three-dimensional instability of a multipolar vortex in a rotating flow. *Phys. Fluids* **12** (11), 2762–2774.

LE DIZÈS, S. 2004 Viscous critical-layer analysis of vortex normal modes. *Stud. Appl. Maths* **112**, 315–332.

LE DIZÈS, S. & LACAZE, L. 2005 An asymptotic description of vortex Kelvin modes. *J. Fluid Mech.* **542**, 69–96.

LE DIZÈS, S. & LAPORTE, F. 2002 Theoretical predictions for the elliptic instability in a two-vortex flow. *J. Fluid Mech.* **471**, 169–201.

LE DIZÈS, S. & VERGA, A. 2002 Viscous interaction of two co-rotating vortices before merging. *J. Fluid Mech.* **467**, 389–410.

LESSEN, M., SINGH, P. J. & PAILLET, F. 1974 The stability of a trailing line vortex. Part 1. Inviscid theory. *J. Fluid Mech.* **63** 753–763.

LEWEKE, T. & WILLIAMSON, C. H. K. 1998 Cooperative elliptic instability of a vortex pair. *J. Fluid Mech.* **360**, 85–119.

LOISELEUX, T., CHOMAZ, J. & HUERRE, P. 1998 The effect of swirl on jets and wakes: linear instability of the Rankine vortex with axial flow. *Phys. Fluids* **10**, 1120–1134.

MEUNIER, P. & LEWEKE, T. 2005 Elliptic instability of a co-rotating vortex pair. *J. Fluid Mech.* **533**, 125–159.

MOORE, D. W. & SAFFMAN, P. G. 1975 The instability of a straight vortex filament in a strain field. *Proc. R. Soc. Lond.* A **346**, 413–425.

PIERREHUMBERT, R. T. 1986 Universal short-wave instability of two-dimensional eddies in an inviscid fluid. *Phys. Rev. Lett.* **57**, 2157–2160.

RYAN, K., THOMPSON, M. C. & HOURIGAN, K. 2005 Three-dimensional transition in the wake of elongated bluff bodies. *J. Fluid Mech.* **538**, 1–29.

SAFFMAN, P. G. 1992 *Vortex Dynamics*. Cambridge University Press.

SIPP, D. & JACQUIN, L. 2003 Widnall instabilities in vortex pairs. *Phys. Fluids* **15**, 1861–1874.

SIPP, D., JACQUIN, L. & COSSU, C. 2000 Self-adaptation and viscous selection in concentrated two-dimensional dipoles. *Phys. Fluids* **12** (2), 245–248.

THOMPSON, M., LEWEKE, T. & PROVANSAL, M. 2001*a* Kinematics and dynamics of sphere wake transition. *J. Fluids Struct.* **15**, 575–585.

THOMPSON, M., LEWEKE, T. & WILLIAMSON, C. 2001*b* The physical mechanism of transition in bluff body wakes. *J. Fluids Struct.* **15**, 607–616.

TSAI, C.-Y. & WIDNALL, S. E. 1976 The stability of short waves on a straight vortex filament in a weak externally imposed strain field. *J. Fluid Mech.* **73**, 721–733.

WALEFFE, F. 1990 On the three-dimensional instability of strained vortices. *Phys. Fluids* A **2** (1), 76–80.